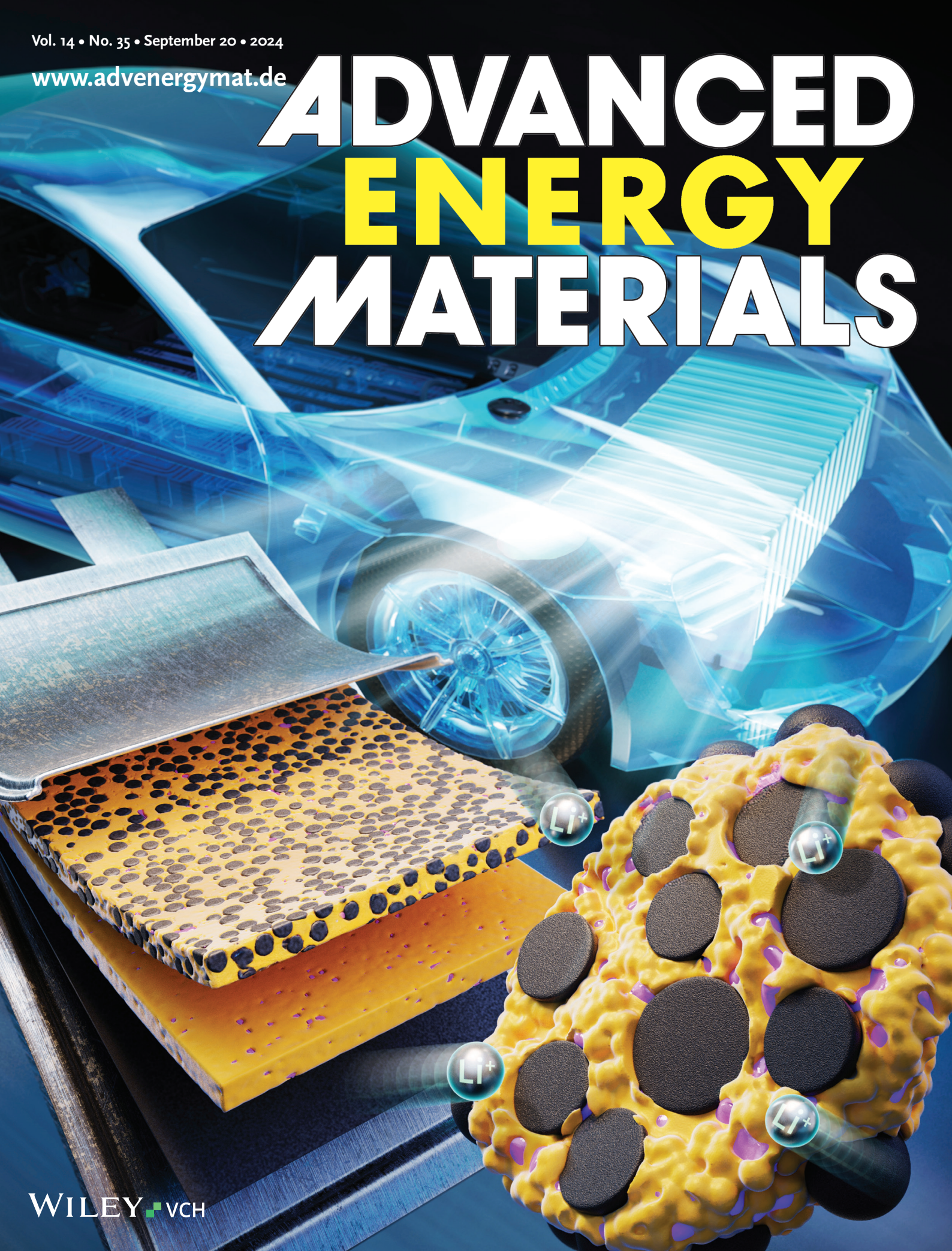


# ADVANCED ENERGY MATERIALS



# Wet-Processable Binder in Composite Cathode for High Energy Density All-Solid-State Lithium Batteries

Seung-Bo Hong, Yoo-Rim Jang, Hun Kim, Yun-Chae Jung, Gyuhwang Shin, Hoe Jin Hah, Woosuk Cho,\* Yang-Kook Sun,\* and Dong-Won Kim\*

Sulfide-based all-solid-state lithium batteries (ASSLBs) are potential alternatives to conventional lithium-ion batteries for enhancing energy density and battery safety. However, the industrial sector encounters technical challenges in the fabrication of high-mass-loaded composite cathodes to improve the energy densities of ASSLBs. Thus, the selection of an appropriate binder and cathode active material is very important for achieving a good cycling performance of ASSLBs. In this study, wet-processable poly(ethylene-co-methyl acrylate-co-glycidyl methacrylate) (EMG) binder and full-concentration gradient (FCG)  $\text{LiNi}_{0.78}\text{Co}_{0.10}\text{Mn}_{0.12}\text{O}_2$  (NCM) cathode active material are employed to fabricate the composite cathode with high active mass loading ( $21.4 \text{ mg cm}^{-2}$ ). The EMG binder provided strong binding properties to the cathode constituents and improved the electrical conductivity of the composite cathode. The FCG NCM mitigated the morphology damages caused by volume changes in the cathode active material during cycling. Consequently, the solid-state lithium battery with the composite cathode employing EMG binder and FCG NCM delivered a high discharge capacity of  $196.6 \text{ mAh g}^{-1}$  corresponding to an areal capacity of  $4.21 \text{ mAh cm}^{-2}$  and showed good capacity retention of 85.1% after 300 cycles at 0.2 C rate and 30 °C.

particularly in light of the flammability of organic materials in commercially available lithium-ion batteries (LIBs), there is a growing need to develop all-solid-state lithium batteries (ASSLBs) using solid electrolytes.<sup>[2–9]</sup> Among the various solid-state electrolytes for ASSLBs, sulfide electrolytes ( $\text{Li}_2\text{S-P}_2\text{S}_5$ ,  $\text{Li}_{10}\text{GeP}_2\text{S}_{12}$ ,  $\text{Li}_6\text{PS}_5\text{X}$ ) have taken center stage owing to their exceptionally high ionic conductivity ( $\approx 10^{-2} \text{ S cm}^{-1}$ ) and ductility, which allow for a large-scale production.<sup>[10–19]</sup> For commercialization of high energy density ASSLBs employing sulfide solid electrolytes, the development of composite cathodes with large active mass loading is critical. The fabrication of composite cathodes for sulfide-based ASSLBs can be categorized into two methods: solvent-free dry processes and wet slurry processes.<sup>[20–24]</sup> When compared to the solvent-free dry-processed electrodes, the cathode components (active material, solid electrolyte, and conducting carbon) can be uniformly dispersed in the

wet-processed composite cathode. In addition, the wet slurry casting method is advantageous for the mass production of large-sized cells and has the benefit of being able to utilize equipment and processes currently used for LIBs.<sup>[25,26]</sup> However, two main obstacles must be overcome to produce a composite cathode with high active mass loading using the slurry casting process for sulfide-based ASSLBs. First, when sulfide solid electrolytes come into contact with organic solvents, the solvent–electrolyte interactions lead to structural collapse and a reduction in the ionic

## 1. Introduction

To address climate change, major industrialized nations have actively developed legislation aimed at restricting the sale of internal combustion engine vehicles to reduce the release of greenhouse gases from vehicles, thus improving air quality in urban environments.<sup>[1]</sup> Consequently, there has been a rapid surge in demand for electric vehicles (EVs). Given the evident limitations of increasing energy density and safety concerns,

S.-B. Hong, G. Shin, D.-W. Kim  
Department of Chemical Engineering  
Hanyang University  
Seoul 04763, South Korea  
E-mail: [dongwonkim@hanyang.ac.kr](mailto:dongwonkim@hanyang.ac.kr)

Y.-R. Jang, Y.-K. Sun, D.-W. Kim  
Department of Battery Engineering  
Hanyang University  
Seoul 04763, South Korea  
E-mail: [yksun@hanyang.ac.kr](mailto:yksun@hanyang.ac.kr)

H. Kim, Y.-K. Sun  
Department of Energy Engineering  
Hanyang University  
Seoul 04763, South Korea

Y.-C. Jung, W. Cho  
Advanced Batteries Research Center  
Korea Electronics Technology Institute  
Gyeonggi 13509, South Korea  
E-mail: [cho4153@keti.re.kr](mailto:cho4153@keti.re.kr)

H. J. Hah  
Battery R&D, LG Energy Solution  
Seoul 07796, South Korea

 The ORCID identification number(s) for the author(s) of this article can be found under <https://doi.org/10.1002/aenm.202400802>

DOI: 10.1002/aenm.202400802

conductivity of the sulfide solid electrolyte. Hence, the choice of solvent in the slurry casting method is limited to solvents with low polarity, such as toluene, xylene, and butyl butyrate.<sup>[27–30]</sup> The second challenge is the restriction of polymer binders. Given the pivotal role of the polymer binder in preserving the structural integrity of cathode components during repetitive volume changes, it is imperative to employ polymer materials with strong adhesive properties. Unfortunately, using highly polar polymers with strong binding is difficult because they cannot be dissolved in less-polar or nonpolar solvents.<sup>[31–33]</sup>

In this study, a composite cathode with improved adhesive and cohesive properties was fabricated using a poly(ethylene-co-methyl acrylate-co-glycidyl methacrylate) (EMG) triblock copolymer. It was dissolved with a solid electrolyte ( $\text{Li}_6\text{PS}_5\text{Cl}$ ) in a low-polarity solvent, and could thus be utilized in the wet slurry process when fabricating composite cathodes. As a cathode active material, a full-concentration gradient (FCG)  $\text{LiNi}_{0.78}\text{Co}_{0.10}\text{Mn}_{0.12}\text{O}_2$  (NCM) was employed, as it could greatly mitigate microcracking during the charge and discharge processes,<sup>[34,35]</sup> which enables it to maintain the morphology stability even under high stack pressure cycling. The solid-state lithium cell assembled with a high-mass-loaded composite cathode employing an EMG binder and FCG NCM cathode active material showed superior cycling performance compared to the cell with the well-known nitrile butadiene rubber (NBR) as a wet-processable binder and conventional NCM material. The detailed mechanism for achieving good cycling characteristics is discussed using various measurements and analyses.

## 2. Results and Discussion

When designing a polymer binder for a composite cathode, the following main characteristics must be considered: flexibility, binding properties, solubility, electrical conductivity, and electrochemical stability.<sup>[36,37]</sup> The chemical structure of the EMG used as a binder in this study is shown in Figure S1 (Supporting Information). The molar ratio of ethylene, methyl acrylate, and glycidyl methacrylate in the EMG terpolymer was 40:4:1. Polyethylene, the predominant component of the terpolymer, imparts sufficient flexibility to the composite cathode.<sup>[38]</sup> The binding properties of EMG stem from the polar groups of poly(methyl acrylate) and poly(glycidyl methacrylate).<sup>[39,40]</sup> The polar carboxylate groups with two oxygen atoms possessing unshared electron pairs can provide strong interactions between the EMG and cathode components. With respect to solubility, EMG was well dissolved in butyl butyrate. To investigate whether butyl butyrate collapses the crystalline structure of  $\text{Li}_6\text{PS}_5\text{Cl}$ , we obtained X-ray diffraction (XRD) patterns of  $\text{Li}_6\text{PS}_5\text{Cl}$  before and after soaking in butyl butyrate and of  $\text{Li}_6\text{PS}_5\text{Cl}/\text{EMG}$  (97/3 by weight) composite prepared by the slurry casting method using butyl butyrate. As shown in Figure S2a (Supporting Information), the XRD pattern of  $\text{Li}_6\text{PS}_5\text{Cl}$  did not change after soaking in butyl butyrate, indicating that it is chemically stable in butyl butyrate that dissolves EMG. XRD pattern of  $\text{Li}_6\text{PS}_5\text{Cl}/\text{EMG}$  composite also confirmed that there were no side reactions between  $\text{Li}_6\text{PS}_5\text{Cl}$  and EMG. In addition, we analyzed Raman spectra of the pristine  $\text{Li}_6\text{PS}_5\text{Cl}$ ,  $\text{Li}_6\text{PS}_5\text{Cl}/\text{NBR}$ , and  $\text{Li}_6\text{PS}_5\text{Cl}/\text{EMG}$  composites. As depicted in Figure S2b (Supporting Information), the major  $\text{PS}_4^{3-}$  peak of  $\text{Li}_6\text{PS}_5\text{Cl}$  remained unchanged after the cast-

ing process of solution containing polymer binder, indicating that both organic solvents and binder are chemically inert during the slurry mixing and drying processes. Moreover, the electrical conductivity of the composite cathode including the polymer binder should be considered. It is imperative to consider the spatial distribution of the binder in a composite cathode, particularly concerning the preservation of ionic and electronic conduction pathways. Owing to the insulating nature of polymer materials, it is essential to distribute the binder in a manner that does not disrupt the conductive pathways.<sup>[41]</sup> The cross-sectional scanning electron microscopy (SEM) images with energy dispersive X-ray spectroscopy (EDS) mapping of the composite cathode were obtained to investigate the distribution of polymer binder (Figure 1a,b). The cathode active material used in this study, FCG NCM, consists of radially oriented rod-shaped primary particles (Figure S3, Supporting Information) with an outward direction a–b plane. Accordingly, it minimizes volume changes that lead to microcracking.<sup>[34,35]</sup> To analyze the distribution of the polymer binder by the signal of carbon (red in the EDS image), a composite cathode was prepared using active material, solid electrolyte, and polymer binder without conductive carbon. The degree to which the polymer binder infiltrates the active material– $\text{Li}_6\text{PS}_5\text{Cl}$  interface is known to directly correlate with the obstruction of the conduction pathway. According to the previous report,<sup>[33]</sup> it was not good for the active material to be completely covered by the binder, since full coverage of the binder on the active material would interfere the ionic and electronic conduction. The cross-sectional EDS mapping images revealed that the EMG binder was locally concentrated at the interface, unlike the NBR. According to the particle size distribution shown in Figure 1c, NBR had a more expanded chain conformation in the polymer solution, indicating that it occupied a larger interfacial area when the composite cathode was prepared from the solution. This large coverage of the NBR binder on the active material blocked electrical conduction pathways in the composite cathode. In contrast, EMG chains with small sizes are more aggregated within the composite cathode, resulting in less hindrance of the electrical conduction pathways. To confirm this hypothesis, the electrochemical characteristics of the composite cathodes were investigated using the galvanostatic intermittent titration technique (GITT) (Figure 1d).<sup>[42]</sup> The diffusion coefficients of the  $\text{Li}^+$  ions ( $D_{\text{Li}^+}$ ) estimated from the GITT results are given in Figure 1e. Considering that the polymer binder is an insulating material,  $D_{\text{Li}^+}$  can be regarded as an indicator of the extent to which the polymer infiltrates the cathode active material– $\text{Li}_6\text{PS}_5\text{Cl}$  interface. As depicted in the figure, the composite cathode with EMG showed higher  $D_{\text{Li}^+}$  values than the NBR-based cathode, providing evidence of less obstruction of  $\text{Li}^+$  ion transport in the presence of the EMG binder. In addition, the ionic and electronic conductivities of the composite cathode were measured by assembling a symmetric SUS/composite cathode/SUS cell and performing AC impedance measurements.<sup>[43,44]</sup> The resulting AC impedance spectra are shown in Figure S4 (Supporting Information), and the calculated electrical conductivities are shown in Figure 1f. Notably, the EMG-based composite cathode exhibited higher electronic and ionic conductivities than the NBR-based electrode. Because there is no difference in the content of the conducting carbon and solid electrolyte in the cathode, the presence of the NBR binder surrounding the active materials may function as a

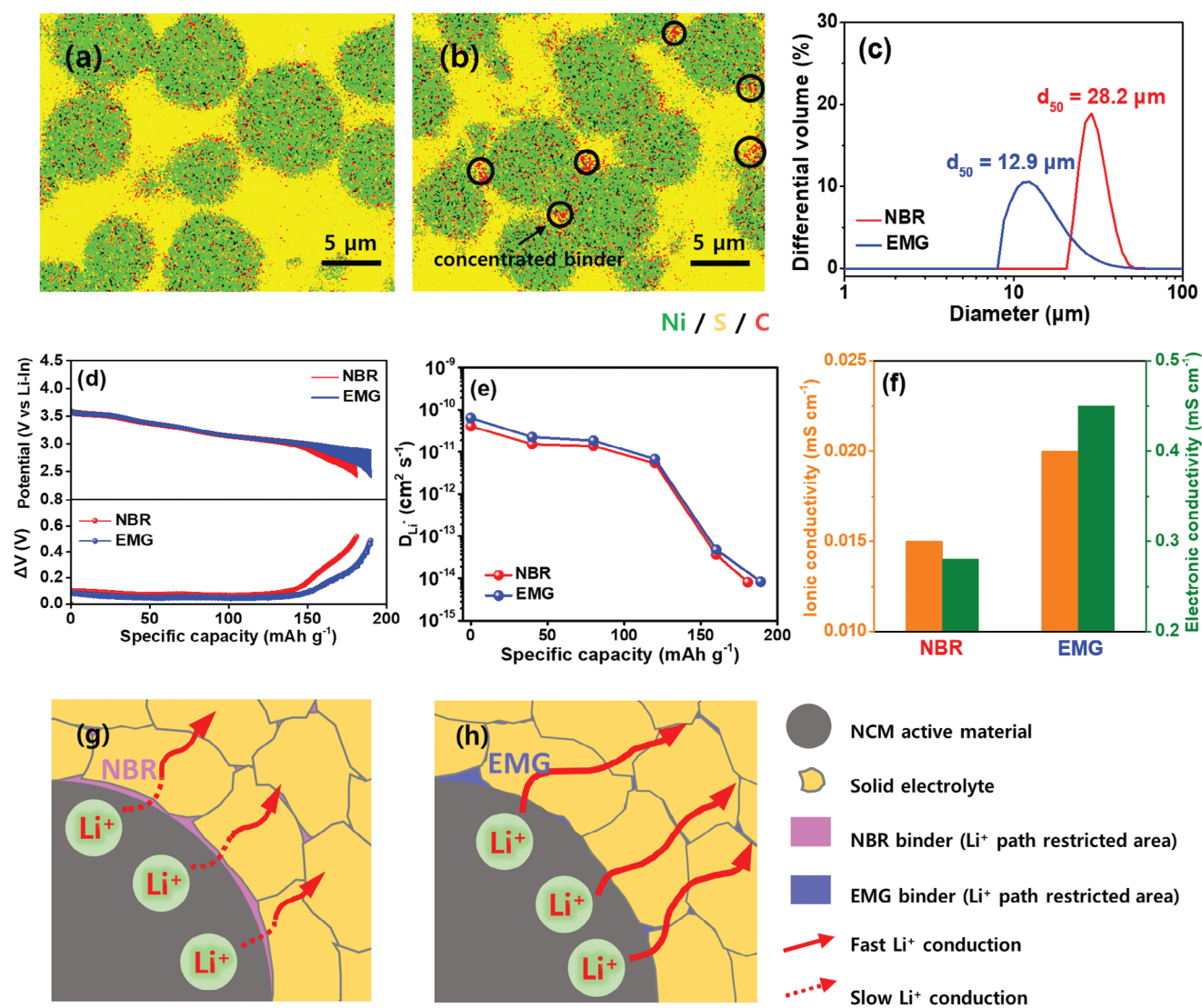


**Figure 1.** EDS-mapping images of cross-sectional composite cathodes prepared with a) NBR and b) EMG. c) Particle size distribution and average diameter of polymer in a binder solution. d) Voltage profiles and polarization curves of the cells were obtained using GITT. e) Diffusion coefficient of  $\text{Li}^+$  estimated from GITT. f) Ionic and electronic conductivities of composite cathodes employing different binders. Schematic illustration of binder distribution and  $\text{Li}^+$  diffusion pathways in the composite cathodes with g) NBR and h) EMG.

direct obstacle to electronic and ionic conduction.<sup>[29]</sup> Based on these results, the localized distribution of EMG ensures that the direct contact between the FCG NCM active material and the solid electrolyte remains intact, resulting in the high electrical conductivity of the composite cathode, as schematically demonstrated in Figure 1g,h. Finally, the electrochemical stability of the EMG binder was investigated by cyclic voltammetry.<sup>[23,27]</sup> It was confirmed from the cyclic voltammograms of  $\text{Li}_6\text{PS}_5\text{Cl}$ -binder composites (Figure S5, Supporting Information) that both NBR and EMG binders are electrochemically stable up to 4.3 V versus  $\text{Li}/\text{Li}^+$ , which is the high voltage limit of the solid-state cell.

A cross-cut adhesion test was performed to evaluate the adhesive strength between the composite cathode and Al current collector (Figure 2a). This was conducted by applying adhesive tape to the composite cathode that was pre-cut into 100 sections and peeling it off from the electrode. The number of sections

that remained attached after the test was related to the adhesion strength between the cathode and the current collector. For the NBR-based composite cathode, most sections ( $\approx 90$ ) were completely peeled off (Figure 2b). In contrast, fewer than 20 sections were peeled off in the EMG-based composite cathode (Figure 2c), confirming that the adhesion strength between the EMG-based cathode and the current collector was much higher. Moreover, the surface and interfacial cutting analysis system (SAICAS) was used in two modes, constant load and constant velocity (Figure 2d,f), to compare the adhesive and cohesive properties of the composite cathodes, respectively.<sup>[45,46]</sup> As presented in Figure 2e,g, the horizontal forces required to sever the EMG-based cathode are greater than those required for the NBR-based cathode in both modes, indicating the superior adhesive and cohesive strengths of the EMG-based composite cathode. The mechanical properties of the composite cathodes were further

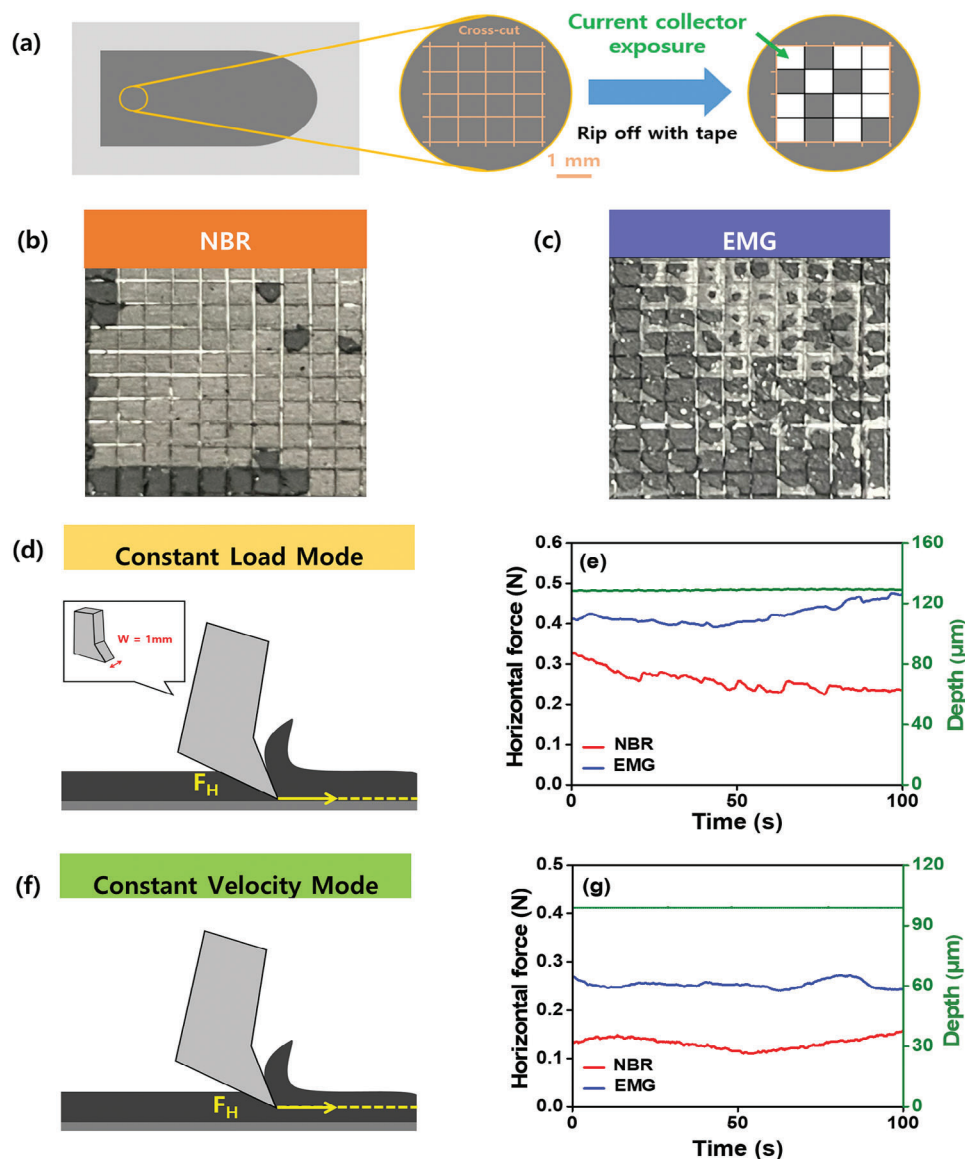


**Figure 2.** a) Schematic illustration of the cross-cut adhesion test and the resulting images of the composite cathodes employing b) NBR and c) EMG after the adhesion test. Schematic presentation of the SAICAS test and the results at d,e) with constant load mode and f,g) constant velocity mode.

evaluated using nanoindentation and nano scratch tests.<sup>[47,48]</sup> Figure S6a,b (Supporting Information) respectively show schematics of the nanoindentation and load–depth curves of the composite cathodes obtained by nanoindentation. When the tip penetrated the composite cathode, the EMG-based cathode exhibited a smaller penetration depth owing to its superior mechanical properties. In addition, the nano scratch test results revealed that the EMG-based cathode had more robust properties than the NBR-based electrode, as shown in Figure S6c,d (Supporting Information).

To further investigate the binding properties of polymer binders on the NCM and  $\text{Li}_6\text{PS}_5\text{Cl}$  surfaces, we conducted density functional theory (DFT) calculations. Computational details are given in Supporting Information. As the key functional groups to interact with the surfaces, the carbonyl oxygen atoms

in the EMG (Figure 3a) and nitrogen atom in the NBR (Figure 3b) were identified as the primary interacting sites with Li atoms on NCM(003) and  $\text{Li}_6\text{PS}_5\text{Cl}(001)$  surfaces (Figure 3c–h; Figure S7, Supporting Information).<sup>[49]</sup> DFT results given in Figure 3i show that the methyl acrylate (MA) and glycidyl methacrylate (GM) groups in EMG have binding energies of  $-0.24$  and  $-1.41$  eV on the NCM(003). In comparison, the nitrile in NBR exhibits a weaker binding energy of  $-0.26$  eV on the NCM(003). On the  $\text{Li}_6\text{PS}_5\text{Cl}(001)$  surface, the binding energies of MA and GM are found to be  $-0.93$  and  $-1.14$  eV, which are much stronger than the binding energy of nitrile ( $-0.69$  eV) in the NBR, as presented in Figure 3j. The strong binding energies of EMG on both NCM and  $\text{Li}_6\text{PS}_5\text{Cl}$  surfaces can be attributed to the high electronic interactions between the EMG and the surfaces of cathode components.<sup>[50]</sup> Bader charge analysis shows that the charge

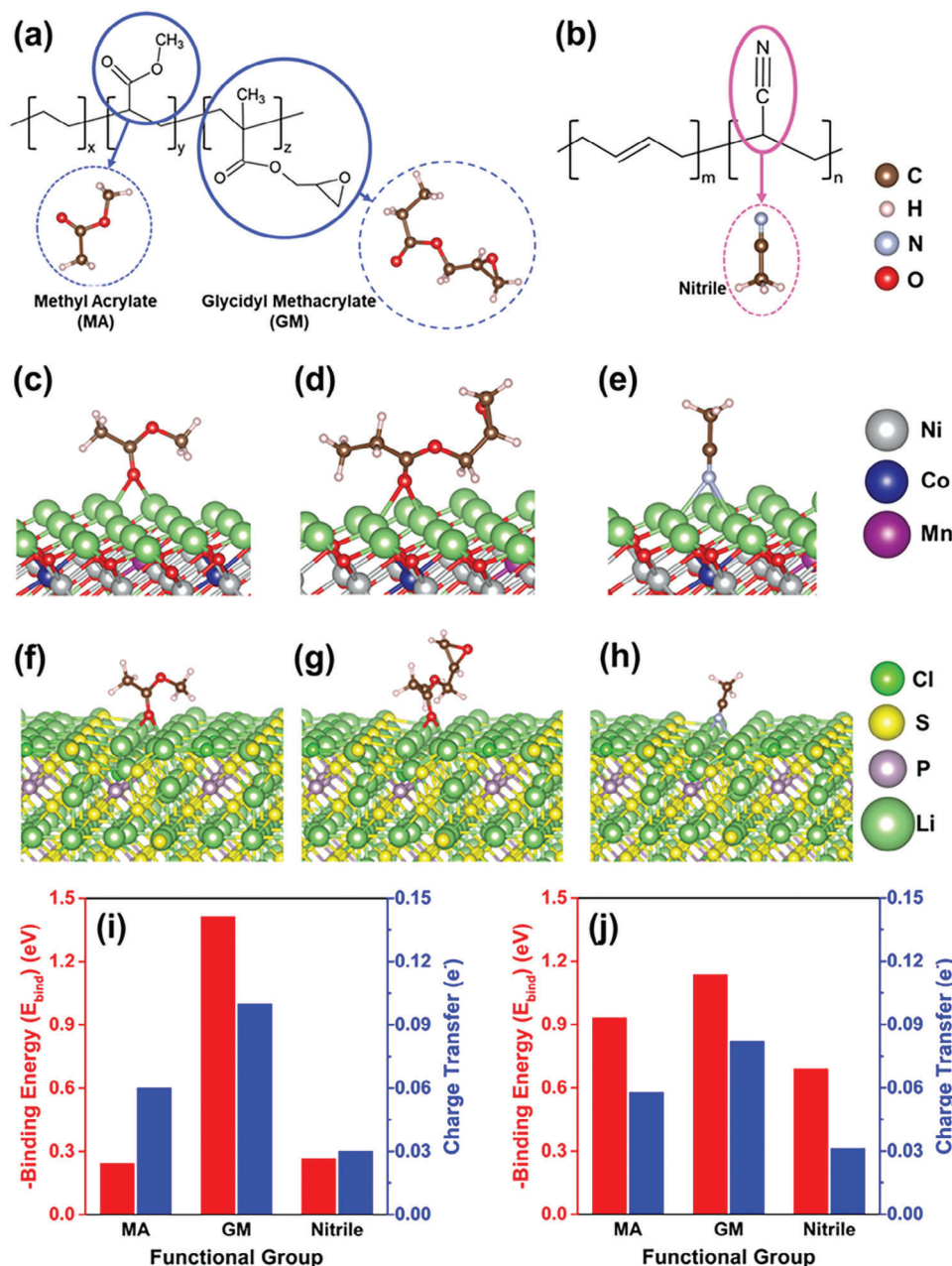


**Figure 3.** Key functional groups in a) EMG and b) NBR for DFT calculations. The most stable binding configuration of c) MA, d) GM, and e) nitrile groups on NCM(003) surface. The most stable binding configuration of f) MA, g) GM, and h) nitrile groups on Li<sub>6</sub>PS<sub>5</sub>Cl(001) surface. The binding energy and charge transfer from the surface to the functional groups on i) NCM(003) and j) Li<sub>6</sub>PS<sub>5</sub>Cl(001) surface.

transfers of 0.06 and 0.10 e<sup>-</sup> occur from the NCM(003) to MA and GM, respectively.<sup>[51]</sup> In the case of Li<sub>6</sub>PS<sub>5</sub>Cl(001), the charge transfers of 0.06 and 0.08 e<sup>-</sup> occur from the Li<sub>6</sub>PS<sub>5</sub>Cl(001) to MA and GM, respectively. However, charge transfers of only 0.03 e<sup>-</sup> occur from both NCM(003) and Li<sub>6</sub>PS<sub>5</sub>Cl to nitrile. These results demonstrate that the cathode components are strongly bonded to EMG rather than NBR.

The cycling performance of the all-solid-state cells was evaluated to investigate the effect of binder on the composite cathode. **Figure 4a** presents the initial charge and discharge curves of the

cells with composite cathodes employing different binders during the pre-conditioning cycle at 0.05 C and 30 °C. The EMG-based cell delivered a slightly higher discharge capacity than that of the NBR-based cell based on cathode active material (196.6 vs 194.0 mAh g<sup>-1</sup>), which corresponded to 4.21 mAh cm<sup>-2</sup>. **Figure 4b** presents the voltage curves of these cells at 0.2 C and 30 °C, and their cycling performance is compared in **Figure 4c**. These figures demonstrate that the EMG-based cell exhibited superior cycling performance compared to the NBR-based cell in terms of discharge capacity and cycling stability. With respect to

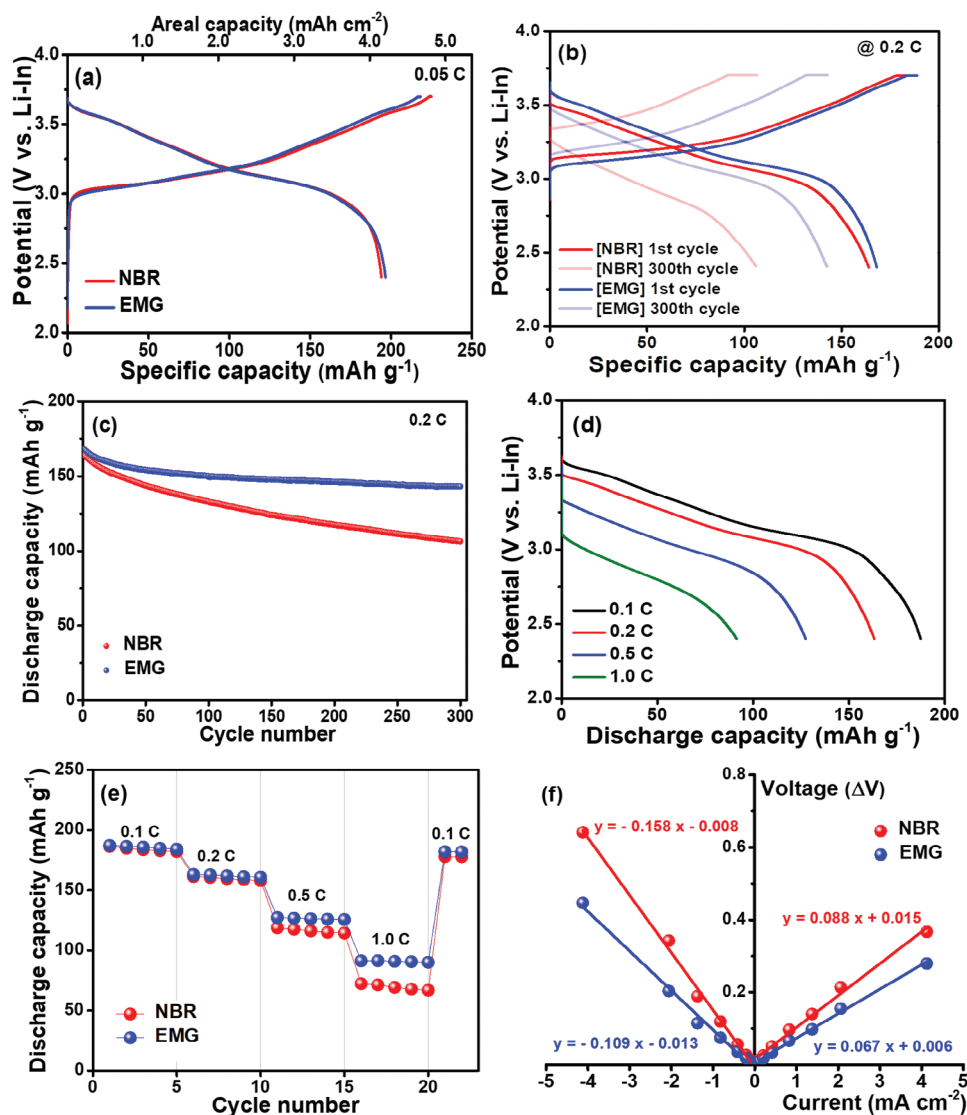


**Figure 4.** a) Voltage curves of the cells during preconditioning cycle at 0.05 C and 30 °C. b) Cycling curves of the cells with different binders at 0.2 C and 30 °C. c) Discharge capacities of the cells with cycle number at 0.2 C and 30 °C. d) Discharge curves of the EMG-based cell at different C rates. e) Rate capability of the cells at various current rates. f) Plot of the voltage change versus current density in the cell with different binders.

the rate capability, the cell employing the EMG binder delivered higher discharge capacities at all current rates (Figure 4d,e). DC-IR of the cells was measured from the slope in the plot of voltage change versus current density at different C rates (Figure S10, Supporting Information; Figure 4f).<sup>[52,53]</sup> In Figure 4f, the EMG-based cell showed lower slopes than the NBR-based cell. These lower DC-IR values can be attributed to the higher ionic and electronic conductivities of the EMG-based composite cathode, as discussed previously.

The cross-sectional morphologies of the composite cathodes were investigated before and after 300 cycles. As shown in Figure S11 (Supporting Information), the as-prepared pristine composite electrodes maintained good interfacial contact between the solid electrolytes and active materials. After 300 cycles, both electrodes exhibited well-preserved interfacial contacts at a fully discharged state (Figure 5a,b). The preservation of good interfa-

cial contact can be ascribed to the rod-shaped arrangement of the primary particles in FCG NCM, which allows the suppression of microcracking during repeated cycling.<sup>[54,55]</sup> A unique microstructure of rod-shaped primary particles that are radially oriented in FCG NCM can mitigate the microcrack formation within the cathode particles by effectively dissipating localized strain resulting from anisotropic lattice volume changes during the repeated cycling. However, noticeable differences were observed at the fully charged state, wherein the cathode active materials significantly shrunk owing to the de-intercalation of lithium ions (Figure 5c,d). The NBR-based composite cathode exhibited evident interfacial detachment between the active material and the solid electrolyte, whereas the EMG-based cathode maintained good interfacial contact even after the de-intercalation of Li<sup>+</sup>, which resulted from the superior binding properties of EMG compared to NBR. The effect of the binder content on the

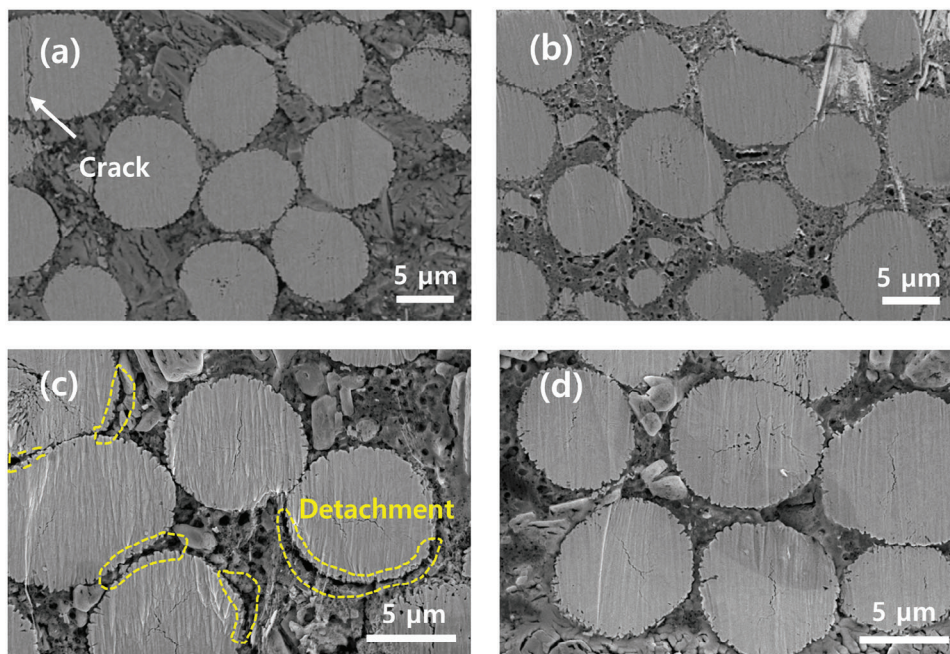


**Figure 5.** Cross-sectional SEM images of the composite cathodes with a) NBR and b) EMG at discharged state after 300 cycles. Cross-sectional SEM images of the composite cathodes with c) NBR and d) EMG at a charged state after 300 cycles.

cycling performance is given in Figure S12 (Supporting Information). It can be seen that the best cycle performance is obtained when the binder content is 2.0 wt.%. When the binder content was 1.0 wt.%, it was not sufficient to bind NCM particles, solid electrolytes, and conductive carbon in the composite cathode. In contrast, the addition of 3.0 wt.% binder reduced the electronic and ionic conductivity of the composite cathode, resulting in inferior cycling performance. These results reveal that the optimum binder content for achieving good cycling performance is 2.0 wt.%. To further study the effect of the binder on the cycling performance at very low binder contents, a composite cathode was prepared with 0.5 wt.% binders. At the cycle at 0.05 C, the type of binder hardly affected the cycling characteristics (Figure S13a, Supporting Information). However, Figure S13b, Supporting Information) reveals that the binder exhibited a significant effect on the cycling stability at 0.2 C, indicating a large difference in the binding ability between the two binders at extremely low binder contents. Moreover, we investigated the effect of the cathode active material on the cycling performance of all-solid-state lithium cells. Instead of FCG NCM, conventional  $\text{LiNi}_{0.8}\text{Co}_{0.1}\text{Mn}_{0.1}\text{O}_2$  (NCM811) was used to prepare the composite cathode. Figure S14a,b (Supporting Information) presents the cycling characteristics of solid-state cells assembled with NCM811 at 0.05 and 0.2 C, respectively, showing the superior cycling performance of the EMG-based cell. The cross-sectional morphology of the NCM811-based composite cathode was investigated. As shown in Figure S14e (Supporting Information), the NCM811 and NBR-based composite cathode exhibited large voids between the active material and solid electrolyte, as well as severe microcracks within the active material after 100 cycles. These voids and microcracks are mitigated in the EMG-based cathode (Figure S14f, Supporting Information). These re-

sults suggest that the NCM811-based cathode shows a large deterioration in the interfacial contact and morphology damage caused by large volumetric fluctuations of the cathode active material when using a polymer binder with poor binding ability. This mechanical degradation of the composite electrode can be overcome to some extent using an EMG binder with superior binding properties.

The mean pressure of the solid-state cells was measured to understand the effect of the binder on cell pressure during charge–discharge cycling.<sup>[56,57]</sup> In this test,  $\text{Li}_4\text{Ti}_5\text{O}_{12}$  (LTO) with zero strain was used as the anode material to consider only the volume changes occurring at the composite cathode. The voltage profiles and pressure changes of the solid-state LTO/FCG NCM cells at 0.2 C rate are shown in Figure S15a,b (Supporting Information). The mean pressure of the cell was obtained from the average values of the highest and lowest pressures during cycling (Figure 6a). The EMG-based cell exhibited a higher mean pressure than the NBR-based cell, indicating that EMG bound to the composite cathode more strongly during repeated cycling. For the successful development of ASSLBs, the cell must operate under low stack pressure. The cell was cycled at a stack pressure of 19 MPa to investigate the role of binder under low-pressure conditions. In the pre-conditioning cycle at 0.05 C, there were slight differences in the cycling behavior (Figure 6b). In contrast, a large capacity reduction was evident in the NBR-based cell after 40 cycles at 0.2 C (Figure 6c). Even when the stack pressure of the cell was readjusted after 70 cycles, the capacity fading continued. In contrast, the EMG-based cell operated stably without noticeable capacity reduction at 19 MPa. To understand the capacity fading mechanism, the charge and discharge curves of the NBR-based cell cycled at 19 MPa are shown in Figure 6d. The increase in the overpotential of the cell was not significant during cycling.

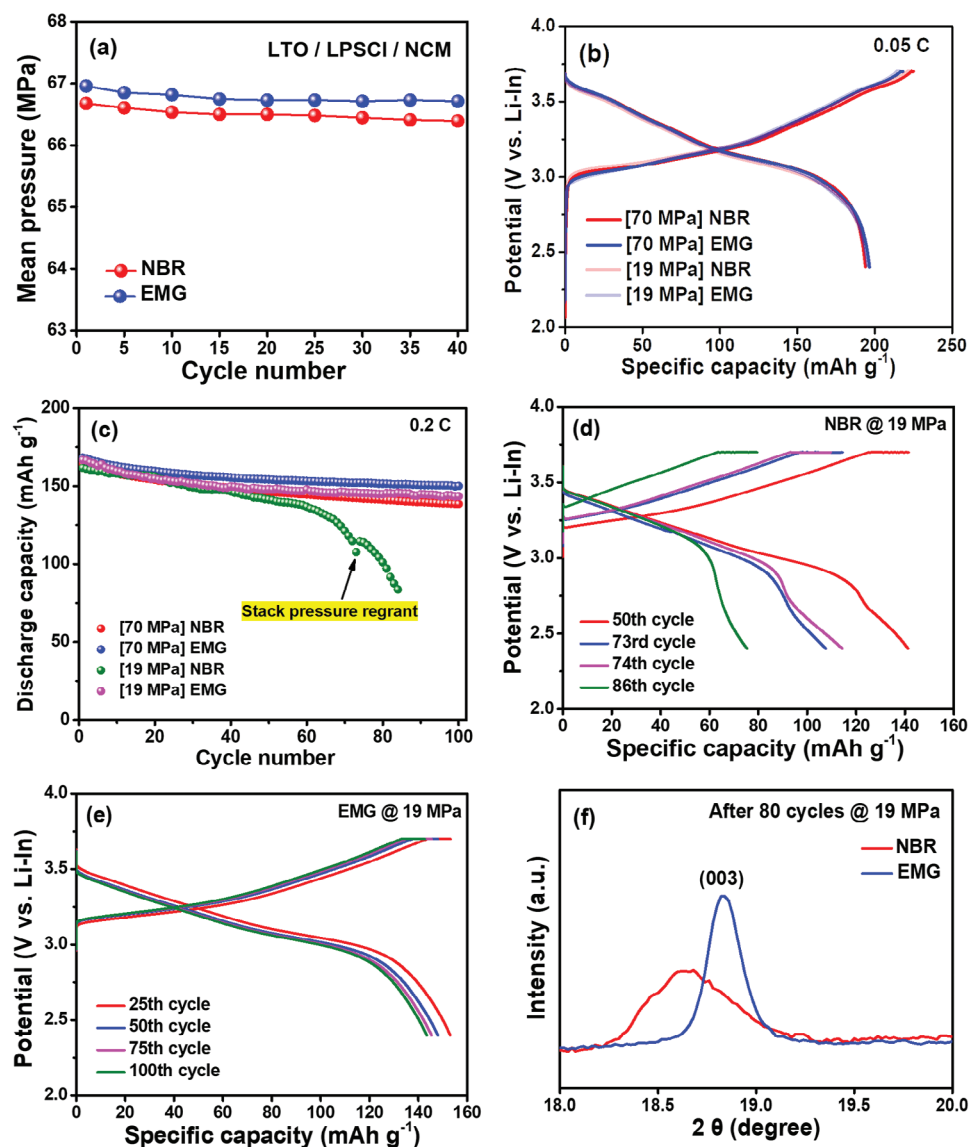


**Figure 6.** a) Mean pressure of the LTO/LPSCI/FCG NCM cells during the repeated cycling at 0.2 C and 30 °C. b) Voltage curves of the solid-state lithium cells at different stack pressure and 0.05 C rate. c) Cycling performance of the cells at different stack pressure and 0.2 C. Charge and discharge curves of the cells with d) NBR and e) EMG at stack pressure of 19 MPa and 0.2 C. f) XRD peaks of the cathodes employing NBR and EMG binders at fully charged state after 80 cycles at 19 MPa stack pressure and 0.2 C.

Instead, the discharge curve dropped abnormally at  $\approx 3.0$  V, unlike in the case of the EMG-based cell (Figure 6e). When a large number of voids are formed at the interface between the active material and the solid electrolyte owing to the inferior binding properties, the restoration of the electrical pathways becomes difficult, resulting in the deterioration of the discharge curve at the end of discharge in the NBR-based cell. The incomplete intercalation of  $\text{Li}^+$  into the active material can be proven by comparing the XRD peak (003) of the cathode at the fully discharged state,<sup>[58–60]</sup> since the (003) peak reflects the c-axis lattice parameter of the active material. As shown in Figure 6f, the asymmetric shape of FCG NCM in the NBR-based cell resulted from the incomplete intercalation of  $\text{Li}^+$ .

EMG binder was applied to the higher active mass-loaded composite cathode (FCG NCM loading:  $32.2 \text{ mg cm}^{-2}$ ). Figure S16a (Supporting Information) presents the initial charge and discharge curves of the cell during the preconditioning cycle at 0.05 C and 30 °C. The composite cathode initially delivered a discharge capacity of  $191.1 \text{ mAh g}^{-1}$ , corresponding to an areal capacity of  $6.15 \text{ mAh cm}^{-2}$ . The capacity retention after 100 cycles was 83.2% at 0.2 C cycling (Figure S16b, Supporting Information).

These results reveal that EMG is a promising wet-processable binder for achieving good cycling performance at high active mass loadings. A practical evaluation of the EMG-based composite cathode was conducted in an anode-less pouch-type full cell

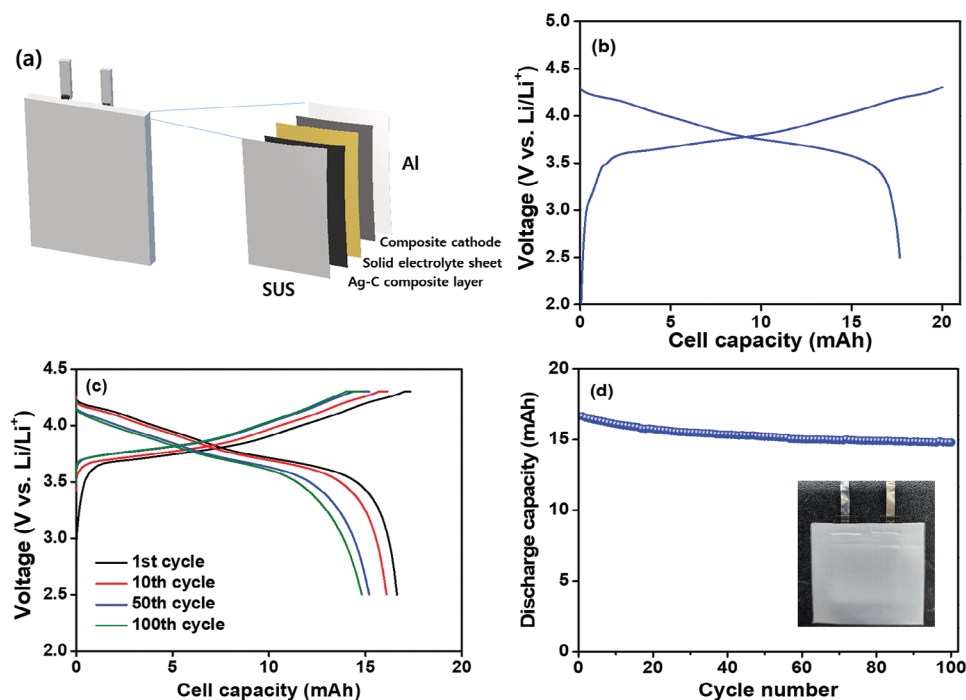


**Figure 7.** a) Anode-less all-solid-state pouch-type cell. b) Voltage profiles of the all-solid-state pouch-type cell with EMG-based composite cathode at 0.05 C and 60 °C. c) Charge and discharge curves and d) cycling performance of the all-solid-state pouch-type cell with EMG-based composite cathode at 0.2 C and 60 °C.

(Figure 7a).<sup>[15,61,62]</sup> The cell was cycled at 60 °C and a low stack pressure of 4 MPa. During cycling at 0.05 C, it delivered a discharge capacity of 17.7 mAh (areal capacity: 4.43 mAh cm<sup>-2</sup>) with an initial Coulombic efficiency of 88.2% (Figure 7b). The gravimetric and volumetric energy densities of the cell were calculated to be 297.0 Wh kg<sup>-1</sup> and 778.0 Wh L<sup>-1</sup>, respectively, as presented in Table S1 (Supporting Information), which is a higher value compared to the energy densities of other all-solid-state batteries reported so far.<sup>[15,41]</sup> At 0.2 C cycling, it exhibited an initial discharge capacity of 16.7 mAh with a capacity retention of 88.9% at the 100th cycle (Figure 7c,d).

Figure 8a and Table S2 (Supporting Information) compare the cycling performance of ASSLBs employing composite cathodes prepared by the wet slurry process.<sup>[28,30,33,63,64]</sup> They revealed that the composite cathode with a high active mass loading, which was prepared by a wet slurry process using EMG and FCG NCM in this study, exhibited the best cycling performance compared to those of other all-solid-state cells reported to date. This improvement in the cycling performance is schematically illustrated in Figure 8b. Unlike the NBR binder, which permeates around the active material and interferes with it, the EMG binder with its high adhesive properties was locally distributed and did not significantly impede the electrical conduction pathways in the composite cathode. With respect to the cathode active material, the rod-shaped FCG NCM may have suppressed the formation of microcracks or void volumes during repeated cycling. The proper combination of the EMG binder and FCG NCM allowed the all-solid-state cell to exhibit good cycling characteristics when applying a wet-processed composite cathode with a high areal capacity to the cell.

### 3. Conclusion

Our study on composite cathodes for ASSLBs provides insight into the selection of a suitable binder and cathode active material for the development of high-mass loaded composite cathodes using the wet-slurry process. The design strategy aims to allow a binder with high adhesive properties to penetrate only to an appropriate extent at the interface between the active material and the solid electrolyte, preventing excessive adsorption of the binder onto the active material. The EMG terpolymer used in this study is well-suited for achieving strong binding properties among the cathode components and maintaining facile electrical conduction pathways. In addition, the use of the FCG NCM reduced the deterioration of the interfacial contacts and morphology damages caused by the volumetric fluctuation of the cathode active material. Consequently, the all-solid-state lithium cell with wet-processed composite cathode with high active mass loading (21.4 mg cm<sup>-2</sup>) exhibited good cycling performance with a capacity retention of 85.1% after 300 cycles at 0.2 C and 30 °C.

### 4. Experimental Section

**Materials:** The solid electrolyte (Li<sub>6</sub>PS<sub>5</sub>Cl, argyrodite, d<sub>50</sub> = 3 μm) was supplied from Jeong Kwan Co., Ltd. Before use, Super C carbon (Timcal) and Li<sub>4</sub>Ti<sub>5</sub>O<sub>12</sub> (MTI) were dried in a vacuum oven at 100 °C for 12 h. EMG and butyl butyrate were purchased from Sigma-Aldrich. NBR was kindly supplied by Kumho Petrochemical. Indium and lithium foils were supplied from Nilaco and Honjo Metal, respectively.

**Synthesis of FCG NCM:** FCG [Ni<sub>0.78</sub>Co<sub>0.10</sub>Mn<sub>0.12</sub>](OH)<sub>2</sub> precursor was synthesized using a previously reported coprecipitation method.<sup>[65]</sup>

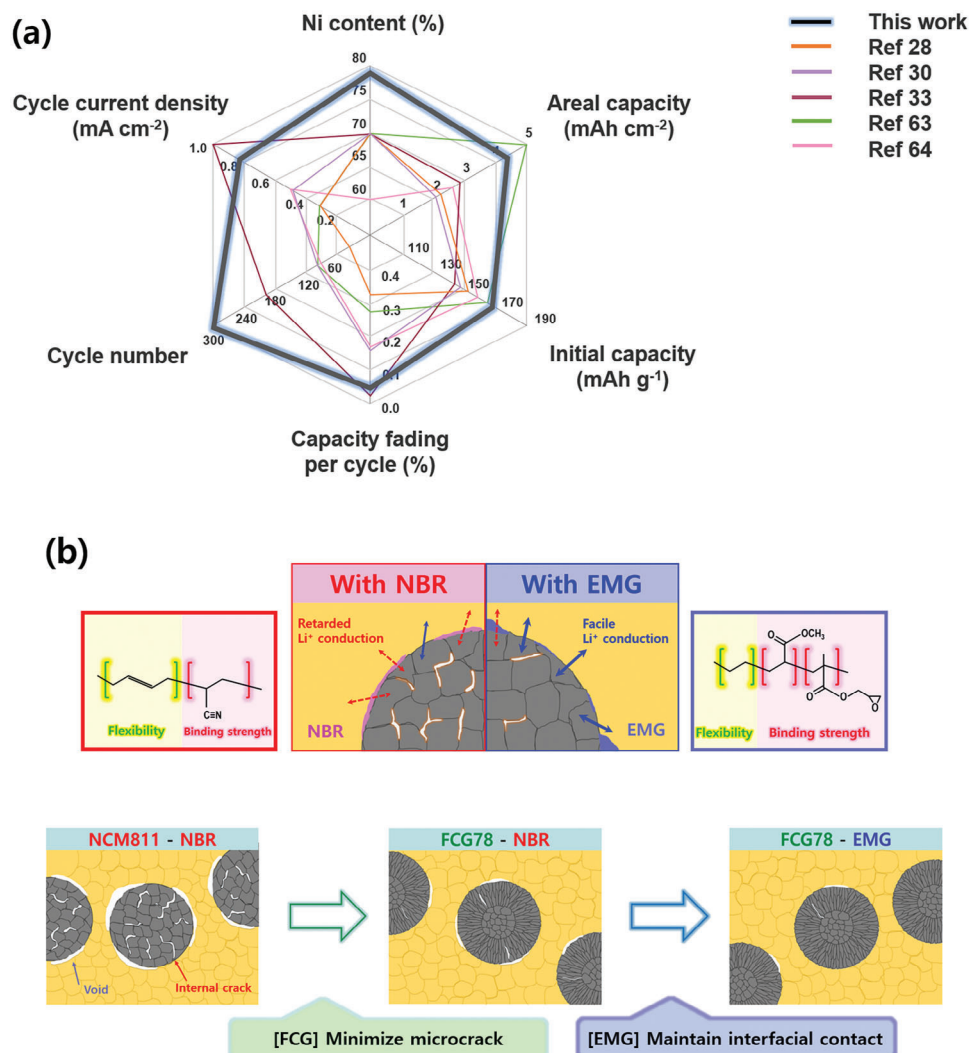


**Figure 8.** a) Comparison of the cycling performance of all-solid-state cells fabricated with composite cathodes using slurry casting wet process. b) Schematic presentation of the composite cathodes prepared with different cathode active materials (NCM811 vs FCG78) and binders (NBR vs EMG).

Initially, 2.0 M NiSO<sub>4</sub>·6H<sub>2</sub>O(aq), 4.0 M NaOH(aq), and 10.5 M NH<sub>4</sub>OH(aq) were separately pumped into a reactor that contained deionized water, NaOH(aq), and NH<sub>4</sub>OH(aq) to form Ni(OH)<sub>2</sub> precipitate. Subsequently, 2.0 M CoSO<sub>4</sub>·7H<sub>2</sub>O(aq) and 2.0 M MnSO<sub>4</sub>·H<sub>2</sub>O(aq) were continuously introduced into 2.0 M NiSO<sub>4</sub>·6H<sub>2</sub>O(aq) as the size of the precipitate increased (the Ni:Co:Mn molar ratio of the metal sulfate solution ranged from 1:0:0 to 73:12.5:14.5). After synthesis, the precipitates were washed, filtered, and dried in a vacuum oven at 110 °C. To obtain the cathode active material, FCG [Ni<sub>0.78</sub>Co<sub>0.10</sub>Mn<sub>0.12</sub>](OH)<sub>2</sub> was mixed with LiOH·H<sub>2</sub>O (molar ratio of Li: (Ni + Co + Mn) = 1.01: 1) and calcined in a tube furnace at 790 °C for 10 h under an O<sub>2</sub> atmosphere.

**Cell Assembly:** The 5 wt.% polymer (NBR or EMG) was dissolved in butyl butyrate solvent to obtain a binder solution. The cathode slurry, comprising the cathode active material, solid electrolyte (Li<sub>6</sub>PS<sub>5</sub>Cl), conductive carbon (Super C), and polymer binder (75.0:21.5:1.5:2.0 by mass) in butyl butyrate, was cast onto the carbon-coated Al foil. The solid content in the cathode slurry was 60 wt.%. The cast cathode slurry was dried under vacuum at 70 °C for 12 h in the glove box. The thickness of the composite cathode after pressing was ≈80 μm. The obtained composite cathode was cut in the shape of a disk with a diameter of 13 mm, and its area was

1.33 cm<sup>2</sup>. The mass loading of active material in the composite cathode was 21.4 mg cm<sup>-2</sup>. For EDS mapping, a composite cathode without conductive carbon was separately prepared using the cathode active material, solid electrolyte, and binder at a mass ratio of 75.0:21.5:2.0. The all-solid-state cell was assembled as follows: First, 150 mg Li<sub>6</sub>PS<sub>5</sub>Cl was pelletized by cold-pressing at 80 MPa. Next, the prepared composite cathode was put on the electrolyte pellet, and both were pressed under 350 MPa. The thickness of the solid electrolyte pellet was ≈700 μm and its ionic conductivity was measured to be 2.1 mS cm<sup>-1</sup> at 30 °C. Third, a Li–In anode was put on the other side of the electrolyte, and a Cu foil was attached to the Li–In anode. The assembled cell was finally pressed at a torque of 11 N m (70 MPa) or 3 N m (19 MPa). A composite anode for pressiometry was prepared using LTO, a solid electrolyte, and conducting carbon in a mass ratio of 60:39:1. The N/P ratio of the cell for the pressiometry was set to 1.3. All the electrode preparation and cell assembly were performed in the high-purity argon gas-filled glove box (MBRAUN). To fabricate a pouch-type solid-state lithium cell with a size of 20 × 20 mm<sup>2</sup>, an Ag–C anode-less electrode was prepared, as reported previously.<sup>[66]</sup> The solid electrolyte sheet was prepared with Li<sub>6</sub>PS<sub>5</sub>Cl and EMG (98:2 by weight) by wet-casting process, and its thickness was 90 μm after pressing. After

applying a vacuum process to the laminate bag, the pouch cell was sealed and pressurized at 490 MPa using a warm isotactic press (WIP; ILSHIN Autoclave) in a dry room (dewpoint below  $-50\text{ }^{\circ}\text{C}$ ). After the WIP process, the obtained pouch cell was placed between pressure jigs and externally pressed at 4 MPa to evaluate its cycling performance.

**Characterization:** The surface and cross-sectional morphology of the composite cathode were examined using field-emission scanning electron microscopy (FE-SEM; Verios G4 UC, FEI) in conjunction with EDS. The composite cathodes were cut using a cross-sectional polisher (IB-19520CCP, JEOL). The particle size distribution of the binder in the polymer solution was determined using a zeta potential and particle size analysis instrument (Otsuka Electronics). XRD measurements were performed using a MiniFlex 600 diffractometer (Rigaku). Raman spectroscopy was conducted using a confocal Raman microscope (Senterra 2, Bruker). The cross-cut adhesion test was performed using an adjustable cutter (TQC Sheen), and the results were organized according to the classification ASTM D3359. The adhesive and cohesive strengths of the composite cathodes were measured using a surface and interfacial cutting analysis system (SAICAS, Daipia Wintes) with a 1 mm-wide diamond blade. Nanoindentation experiments were conducted using a nanoindentation device (NanoTest NTX, Micro Materials). Nanoscratch tests were performed using a NanoTest Vantage (Micro Materials Ltd). The scanning velocity was set at  $10\text{ }\mu\text{m s}^{-1}$  with 0.2-mN topography load and 200-mN scratch load. Pressiometry was performed using a pressure sensor with a maximum 1-ton load scale.

**Electrochemical Measurements:** GITT was performed to measure the diffusion coefficients of  $\text{Li}^+$  ions in the composite electrode at a current density of  $0.41\text{ mA cm}^{-2}$  using a WBCS 3000 (Wonatech).<sup>[23]</sup> The cell was subjected to repeated discharge pulses (60 s), interrupted by 2 h of rest until the potential decreased to 2.4 V. The electronic and ionic conductivities of the composite cathode were measured by electrochemical impedance spectroscopy (600D, CH Instruments) of the SUS/composite cathode/SUS cell in the frequency range of 10–1 MHz, with an amplitude of 10 mV. To investigate the electrochemical stability, cyclic voltammetry was performed using a potentiostat (CHI 660, CH instruments Inc) at a scan rate of  $1\text{ mV s}^{-1}$  and  $30\text{ }^{\circ}\text{C}$ . For the cycling test, the all-solid-state lithium cell was subjected to two preconditioning cycles at 0.05 C ( $1\text{ C} = 4.1\text{ mA cm}^{-2}$ ). Subsequently, it was charged to 3.7 V at 0.2 C, and then further charged at a constant voltage until the current reached 50% of the charging current (0.1 C). It was then discharged to 2.4 V at 0.2 C. The DC-IR of the cells was obtained from the slope of the voltage increment versus the current plot as follows:<sup>[53]</sup> First, the cell was cycled at 0.05 C rate. Subsequently, it was charged up to 3.1 V and left to rest for 1 h. Finally, at progressively higher C rates (ranging from 0.025 to 1 C), the cell underwent a cycle of charging for 10 s, followed by a 20-min rest, discharging for 10 s, and concluding with another 20-min rest period.

## Supporting Information

Supporting Information is available from the Wiley Online Library or from the author.

## Acknowledgements

S.-B.H. and Y.-R.J. contributed equally to this work. This work was supported by LG Energy Solution and the Technology Innovation Program (20012330 and 20024827) funded by the Ministry of Trade, Industry, and Energy (MOTIE, Korea). The authors thank Prof. Kyeonghak Kim for the discussion of DFT calculations.

## Conflict of Interest

The authors declare no conflict of interest.

## Data Availability Statement

The data that support the findings of this study are available from the corresponding author upon reasonable request.

## Keywords

all-solid-state battery, composite cathode, full-concentration gradient cathode, polymer binder, sulfide electrolyte

Received: February 20, 2024

Revised: June 11, 2024

Published online: June 23, 2024

- [1] Z. Yang, H. Huang, F. Lin, *Adv. Energy Mater.* **2022**, *12*, 2200383.
- [2] Q. Wang, P. Ping, X. Zhao, G. Chu, J. Sun, C. Chen, *J. Power Sources* **2012**, *208*, 210.
- [3] D.-J. Yoo, S. Yang, Y. S. Yun, J. H. Choi, D. Yoo, K. J. Kim, J. W. Choi, *Adv. Energy Mater.* **2018**, *8*, 1802365.
- [4] J.-G. Han, C. Hwang, S. H. Kim, C. Park, J. Kim, G. Y. Jung, K. Baek, S. Chae, S. J. Kang, J. Cho, S. K. Kwak, H.-K. Song, N.-S. Choi, *Adv. Energy Mater.* **2020**, *10*, 2000563.
- [5] Y.-K. Liu, C.-Z. Zhao, J. Du, X.-Q. Zhang, A.-B. Chen, Q. Zhang, *Small* **2023**, *19*, 2205315.
- [6] C. Park, J. Lee, S. Lee, Y. J. Han, J. Kim, S.-K. Jung, *Adv. Energy Mater.* **2023**, *13*, 2203861.
- [7] S. Yan, Z. Wang, F. Liu, H. Zhou, K. Liu, *Adv. Funct. Mater.* **2023**, *33*, 2303739.
- [8] H.-Y. Zhou, Y. Ou, S.-S. Yan, J. Xie, P. Zhou, L. Wan, Z.-A. Xu, F.-X. Liu, W.-L. Zhang, Y.-C. Xia, K. Liu, *Angew. Chem., Int. Ed.* **2023**, *62*, 202306948.
- [9] S. Yan, Y. Lu, F. Liu, Y. Xia, Q. Li, K. Liu, *CCS Chem.* **2023**, *5*, 1612.
- [10] Y. Kato, S. Hori, T. Saito, K. Suzuki, M. Hirayama, A. Mitsui, M. Yonemura, H. Iba, R. Kanno, *Nat. Energy* **2016**, *1*, 16030.
- [11] D. Chang, K. Oh, S. J. Kim, K. Kang, *Chem. Mater.* **2018**, *30*, 8764.
- [12] F. Zhao, J. Liang, C. Yu, Q. Sun, X. Li, K. Adair, C. Wang, Y. Zhao, S. Zhang, W. Li, S. Deng, R. Li, Y. Huang, H. Huang, L. Zhang, S. Zhao, S. Lu, X. Sun, *Adv. Energy Mater.* **2020**, *10*, 1903422.
- [13] S. Wang, W. Zhang, X. Chen, D. Das, R. Ruess, A. Gautam, F. Walther, S. Ohno, R. Koerver, Q. Zhang, W. G. Zeier, F. H. Richter, C.-W. Nan, J. Janek, *Adv. Energy Mater.* **2021**, *11*, 2100654.
- [14] J. Woo, Y. B. Song, H. Kwak, S. Jun, B. Y. Jang, J. Park, K. T. Kim, C. Park, C. Lee, K.-H. Park, H.-W. Lee, Y. S. Jung, *Adv. Energy Mater.* **2023**, *13*, 2203292.
- [15] Y.-G. Lee, S. Fujiki, C. Jung, N. Suzuki, N. Yashiro, R. Omoda, D.-S. Ko, T. Shiratsuchi, T. Sugimoto, S. Ryu, J. H. Ku, T. Watanabe, Y. Park, Y. Aihara, D. Im, I. T. Han, *Nat. Energy* **2020**, *5*, 299.
- [16] J. Wu, L. Shen, Z. Zhang, G. Liu, Z. Wang, D. Zhou, H. Wan, X. Xu, X. Yao, *Electrochem. Energy Rev.* **2021**, *4*, 101.
- [17] J. Wu, S. Liu, F. Han, X. Yao, C. Wang, *Adv. Mater.* **2021**, *33*, 2000751.
- [18] Z. Zhang, L. Wu, D. Zhou, W. Weng, X. Yao, *Nano Lett.* **2021**, *21*, 5233.
- [19] X. Zhao, P. Xiang, J. Wu, Z. Liu, L. Shen, G. Liu, Z. Tian, L. Chen, X. Yao, *Nano Lett.* **2023**, *23*, 227.
- [20] K. Lee, S. Kim, J. Park, S. H. Park, A. Coskun, D. S. Jung, W. Cho, J. W. Choi, *J. Electrochem. Soc.* **2017**, *164*, A2075.
- [21] Y. J. Nam, D. Y. Oh, S. H. Jung, Y. S. Jung, *J. Power Sources* **2018**, *375*, 93.
- [22] F. Hippauf, B. Schumm, S. Doerfler, H. Althues, S. Fujiki, T. Shiratsuchi, T. Tsujimura, Y. Aihara, S. Kaskel, *Energy Storage Mater.* **2019**, *21*, 390.
- [23] S.-B. Hong, Y.-J. Lee, U.-H. Kim, C. Bak, Y. M. Lee, W. Cho, H. J. Ahn, Y.-K. Sun, D.-W. Kim, *ACS Energy Lett.* **2022**, *7*, 1092.

- [24] D. Y. Oh, K. T. Kim, S. H. Jung, D. H. Kim, S. Jun, S. Jeoung, H. R. Moon, Y. S. Jung, *Mater. Today* **2022**, *53*, 7.
- [25] J. H. Teo, F. Strauss, D. Tripkovic, S. Schweidler, Y. Ma, M. Bianchini, J. Janek, T. Brezesinski, *Cell. Rep. Phys. Sci.* **2021**, *2*, 100465.
- [26] G. Li, S. Wang, J. Fu, Y. Liu, Z. Chen, *Batteries* **2023**, *9*, 347.
- [27] K. Lee, J. Lee, S. Choi, K. Char, J. W. Choi, *ACS Energy Lett.* **2019**, *4*, 94.
- [28] J. Lee, K. Lee, T. Lee, H. Kim, K. Kim, W. Cho, A. Coskun, K. Char, J. W. Choi, *Adv. Mater.* **2020**, *32*, 2001702.
- [29] K. T. Kim, D. Y. Oh, S. Jun, Y. B. Song, T. Y. Kwon, Y. Han, Y. S. Jung, *Adv. Energy Mater.* **2021**, *11*, 2003766.
- [30] Y.-J. Lee, S.-B. Hong, D.-W. Kim, *J. Ind. Eng. Chem.* **2023**, *122*, 341.
- [31] N. Ripphaus, P. Strobl, B. Stiaszny, T. Zinkevich, M. Yavuz, J. Schnell, S. Indris, H. A. Gasteiger, S. J. Sedlmaier, *J. Electrochem. Soc.* **2018**, *165*, A3993.
- [32] J. Lee, T. Lee, K. Char, K. J. Kim, J. W. Choi, *Acc. Chem. Res.* **2021**, *54*, 3390.
- [33] K. T. Kim, T. Y. Kwon, Y. B. Song, S.-M. Kim, S. C. Byun, H.-S. Min, S. H. Kim, Y. S. Jung, *Chem. Eng. J.* **2022**, *450*, 138047.
- [34] Y.-K. Sun, Z. Chen, H.-J. Noh, D.-J. Lee, H.-G. Jung, Y. Ren, S. Wang, C. S. Yoon, S.-T. Myung, K. Amine, *Nat. Mater.* **2012**, *11*, 942.
- [35] K.-J. Park, H.-G. Jung, L.-Y. Kuo, C. S. Yoon, Y.-K. Sun, *Adv. Energy Mater.* **2018**, *8*, 1801202.
- [36] F. Zou, A. Manthiram, *Adv. Energy Mater.* **2020**, *10*, 2002508.
- [37] D. Cao, Y. Zhao, X. Sun, A. Natan, Y. Wang, P. Xiang, W. Wang, H. Zhu, *ACS Energy Lett.* **2020**, *5*, 3468.
- [38] Q. Yang, X. Chen, Z. He, F. Lan, H. Liu, *RSC Adv.* **2016**, *6*, 12053.
- [39] L.-L. Zhao, J.-J. Su, J. Han, B. Zhang, L. Ou, *RSC Adv.* **2017**, *7*, 23065.
- [40] K. Haggag, M. A. A. E. Ghaffar, F. A. Kantouch, A. I. Hashem, A. A. Ramadan, Z. M. Mahmoud, *J. Appl. Sci. Res.* **2012**, *8*, 5169.
- [41] D. Cao, Q. Li, X. Sun, Y. Wang, X. Zhao, E. Cakmak, W. Liang, A. Anderson, S. Ozcan, H. Zhu, *Adv. Mater.* **2021**, *33*, 2105505.
- [42] J. S. Horner, G. Whang, D. S. Ashby, I. V. Kolesnichenko, T. N. Lambert, B. S. Dunn, A. A. Talin, S. A. Roberts, *ACS Appl. Energy Mater.* **2021**, *4*, 11460.
- [43] P. Minnmann, L. Quillman, S. Burkhardt, F. H. Richter, J. Janek, *J. Electrochem. Soc.* **2021**, *168*, 040537.
- [44] T. Asano, S. Yubuchi, A. Sakuda, A. Hayashi, M. Tatsumisago, *J. Electrochem. Soc.* **2017**, *164*, A3960.
- [45] S. Byun, Y. Roh, K. M. Kim, M.-H. Ryou, Y. M. Lee, *Appl. Mater. Today* **2020**, *21*, 100809.
- [46] H. Kim, H.-N. Choi, J.-Y. Hwang, C. S. Yoon, Y.-K. Sun, *ACS Energy Lett.* **2023**, *8*, 3971.
- [47] J. Oh, S. H. Choi, J. Y. Kim, J. Lee, T. Lee, N. Lee, T. Lee, Y. Sohn, W. J. Chung, K. Y. Bae, S. Son, J. W. Choi, *Adv. Energy Mater.* **2023**, *13*, 2301508.
- [48] J.-Y. Choi, D. J. Lee, Y. M. Lee, Y.-G. Lee, K. M. Kim, J.-K. Park, K. Y. Cho, *Adv. Funct. Mater.* **2013**, *23*, 2108.
- [49] A. A. Khan, I. Muhammad, R. Ahmad, I. Ahmad, N. Ullah, *J. Power Sources* **2023**, *580*, 233358.
- [50] S. Jia, R. Wang, F. Liu, H. Huo, J. Zhou, L. Li, *Mater. Adv.* **2024**, *5*, 3696.
- [51] R. Shi, S. Qian, D. Zhao, C. Shi, C. He, J. Sha, E. Liu, N. Zhao, *Phys. E.* **2022**, *142*, 115260.
- [52] K. Yamamoto, D. Suemasa, K. Masuda, K. Aita, T. Endo, *ACS Appl. Mater. Interfaces* **2018**, *10*, 6346.
- [53] D. Zhang, B. S. Haran, A. Durairajan, R. E. White, Y. Podrazhansky, B. N. Popov, *J. Power Sources* **2000**, *97*, 122.
- [54] S. H. Jung, U.-H. Kim, J.-H. Kim, S. Jun, C. S. Yoon, Y. S. Jung, Y.-K. Sun, *Adv. Energy Mater.* **2020**, *10*, 1903360.
- [55] J. H. Lee, C. S. Yoon, J.-Y. Hwang, S.-J. Kim, F. Maglia, P. Lamp, S.-T. Myung, Y.-K. Sun, *Energy Environ. Sci.* **2016**, *9*, 2152.
- [56] H. Lim, S. Jun, Y. B. Song, H. Bae, J. H. Kim, Y. S. Jung, *Energy Storage Mater.* **2022**, *50*, 543.
- [57] H.-J. Shin, J. T. Kim, A.-Y. Kim, N. Noh, J. Park, C. R. Park, S. Yu, H. Kim, K. Y. Chung, J. M. Yuk, S.-T. Myung, H.-G. Jung, *Adv. Energy Mater.* **2023**, *13*, 2301220.
- [58] H.-H. Ryu, B. Namkoong, J.-H. Kim, I. Belharouak, C. S. Yoon, Y.-K. Sun, *ACS Energy Lett.* **2021**, *6*, 2726.
- [59] Y. Han, S. H. Jung, H. Kwak, S. Jun, H. H. Kwak, J. H. Lee, S.-T. Hong, Y. S. Jung, *Adv. Energy Mater.* **2021**, *11*, 2100126.
- [60] C. Wei, C. Yu, S. Chen, S. Chen, L. Peng, Y. Wu, S. Li, S. Cheng, J. Xie, *Electrochim. Acta* **2023**, *438*, 141545.
- [61] J. Oh, S. H. Choi, B. Chang, J. Lee, T. Lee, N. Lee, H. Kim, Y. Kim, G. Im, S. Lee, J. W. Choi, *ACS Energy Lett.* **2022**, *7*, 1374.
- [62] W.-Z. Huang, Z.-Y. Liu, P. Xu, W.-J. Kong, X.-Y. Huang, P. Shi, P. Wu, C.-Z. Zhao, H. Yuan, J.-Q. Huang, Q. Zhang, *J. Mater. Chem. A.* **2023**, *11*, 12713.
- [63] J. Lee, J. W. Choi, *Ecomat* **2022**, *4*, e12193.
- [64] D. Y. Oh, Y. J. Nam, K. H. Park, S. H. Jung, K. T. Kim, A. R. Ha, Y. S. Jung, *Adv. Energy Mater.* **2019**, *9*, 1802927.
- [65] G.-T. Park, H.-H. Ryu, T.-C. Noh, G.-C. Kang, Y.-K. Sun, *Mater. Today* **2022**, *52*, 9.
- [66] Y.-C. Jung, C. Hwang, M.-J. Kwak, S.-J. Jeon, Y. J. Lee, W.-J. Kwak, H.-S. Kim, W. Cho, J.-S. Yu, *J. Mater. Chem. A.* **2023**, *11*, 25275.